Johan Christian Jenssen

Numerical simulation of cavitation on a reversible pump turbine with pre-rotation

Master's thesis in Mechanical Engineering
Supervisor: Pål-Tore Selbo Storli
July 2020

NTNU
Norwegian University of
Science and Technology

Johan Christian Jenssen

Numerical simulation of cavitation on a reversible pump turbine with pre-rotation

NTNU
Innovation and Creativity

Dedicated to

the Waterpower Lab

Preface

This master's thesis is the author's work during the final semester at the Water-power Laboratory, Department of Energy and Process Engineering (EPT) at the Norwegian University of Science and Technology (NTNU) in Trondheim, Norway. Associate Professor Pål-Tore Selbo Storli was the main supervisor during this master's thesis.
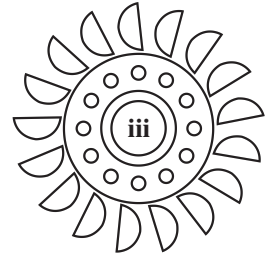
Abstract

In order to reduce the effect of global warming, the CO_2 emissions needs to be reduced considerably. A solution is to increase the capacity of renewables. Pumped hydropower storage (PHS) is the most common way to stabilise the power grid and is increasingly important with the increase in intermittent renewables. Norway has a lot of potential for PHS. An option is retrofitting a reversible pump turbine (RPT) in an existing hydropower plant. The RPT is likely to experience unwanted cavitation in pump mode of operation when it replaces a turbine. A proposed solution is to add a booster pump upstream of the RPT which increases the inlet pressure and therefore reduce or eliminate cavitation. The booster pump might produce pre-rotation at the inlet of the RPT. The effect pre-rotation has on the cavitation performance of the RPT is investigated in this thesis.

Steady-state multiphase CFD simulations of an existing RPT in pump mode of operation were performed with pre-rotation. Three operating points near the best efficiency point (BEP) was simulated without pre-rotation in addition to four different pre-rotations. The pre-rotation was based on a simplification of an axial booster pump as the inlet condition of the CFD simulation. It was found that the pre-rotation had a significant impact on the cavitation performance, especially at the "high Q" operating point ($Q/Q_{BEP} = 1.1293$). For this operating point, the pre-rotation with the best cavitation performance (the lowest σ_R) was found to be negative pre-rotation (NPR) which reduced the σ_R with up to 25.2%. NPR is pre-rotation in the opposite direction as the impeller and positive pre-rotation (PPR) is the other way around. PPR for this operating point increased the σ_R significantly with up to 93% compared to no pre-rotation. Pre-rotation effected the other operating points in an insignificant amount compared to the high Q operating point.

NPR applied at the inlet of the RPT is increases the head and PPR reduces the

head of the RPT. For the simulated operation points, it was also found that all the simulated pre-rotations reduced the efficiency of the RPT.

Sammendrag

For å redusere effekten av klimaendringene, må CO2 utslippene reduseres betraktelig. En løsning er å øke kapasiteten av fornybare energikilder. Pumpekraftverk er i dag en av de vanligste metodene for å stabilisere strømnettet og vil ha en nøkkelrolle når strømnettet i større grad skal forsynes med en økning av variable fornybare energikilder. Norge har stort potensialet for å bygge ut pumpekraftverk. En mulighet er å erstatte en turbin i et eksisterende kraftverk med en reversibel pumpeturbin. Gjennomføres dette, er det forventes at pumpeturbinen vil bli utsatt for uønsket kavitasjon når den er i pumpemodus. En foreslått løsning er å montere en boosterpumpe oppstrøms for pumpeturbinen. Dette øker innløpstrykket til pumpeturbinen og redusere eller eliminere kavitasjonen. Boosterpumpen kan produsere en pre-rotasjon ved innløpet til pumpeturbinen. Hvordan pre-rotasjon påvirker kavitasjonsegenskapene til pumpeturbinen undersøkes i denne oppgaven.

Stasjonære multifase CFD simuleringer av en eksisterende pumpende pumpeturbin med pre-rotasjon ble utført. Tre driftspunkter ble simulert i nærheten av driftspunket med beste virkningsgrad. Dette ble gjort med fire forskjellige pre-rotasjonen i tillegg til uten pre-rotasjon. Pre-rotasjonen var basert på en forenkling av en axial boosterpumpe og ble brukt som innløpsbetingelse i CFD simuleringen. Fra simuleringene ble det kjent at pre-rotasjon hadde signifikant virkning på pumpeturbinens kavitasjons egenskaper, i spesielt stor grad ved driftspunktet $Q/Q_{BEP} = 1.1293$. For dette driftspunktet var pre-rotasjonen som førte til de beste kavitasjonsegenskapene (laveste σ_R) negativ i forhold til løpehjulets rotasjons retning og reduserte σ_R med opptil 25.2%. Positiv pre-rotasjon er definert motsatt rettet av negativ pre-rotasjon. Under simuleringene med positiv pre-rotasjon observeres det at σ_R økte betraktelig, opp til 93% i forhold til simuleringene uten pre-rotasjon. Pre-rotasjon hadde vesentlig mindre effekt på kavitasjonsegenskapene ved de andre driftspunktene.

Negativ pre-rotasjon ved innløpet til pumpeturbinen økte løftehøyden til pumpeturbinen. Positiv pre-rotasjon reduserer løftehøyden til pumpeturbinen. For de simulerte driftspunktene ble det observert at alle pre-rotasjonene reduserte pumpeturbienens virkningsgrad.

Acknowledgements

Contents

List of Tables

List of Figures

List of Symbols

Latin symbols

A	Area	(m^2)
c	Absolute velocity	$(m\ s^{-1})$
D	Reference diameter	(m)
E	Specific energy	$(J\ kg^{-1})$
g	Gravitational acceleration	$(m\ s^{-2})$
H	Head; column height of water	(m)
H_t	Theoretical head	(m)
$\dot{m}$	Mass flow	$(kg\ s^{-1})$
m	Mass	(kg)
n	Rotational speed	(s^{-1})
$NSPH$	Net Positive Suction Head	(m)
n_{ED}	Speed factor	$(-)$
n_s	Specific speed	$(-)$
p	Pressure, apparent order of a method	$(Pa), (-)$
p_{va}	Vapor pressure	(Pa)
P_h	Hydraulic power	(W)

P_m	Mechanical power	(W)
Q	Volumetric discharge	$(m^3\ s^{-1})$
Q_{ED}	Discharge factor	$(-)$
Re	Reynolds number	$(-)$
T	Torque	(Nm)
t	Time	(s)
u	Peripheral velocity	$(m\ s^{-1})$
w	Relative velocity	$(m\ s^{-1})$
y^+	Dimensionless wall distance	$(-)$

Greek symbols

α_{GV}	Guide vane angle	$(°)$
η_h	Hydraulic efficiency	$(-)$
ε	Error	$(-)$
μ	Dynamic viscosity	$(kg\ m^{-1}\ s^{-1})$
ν	Kinematic viscosity	$(m^2\ s^{-1})$
ρ	Density	$(kg\ m^{-3})$
σ	Thoma cavitation factor	$(-)$

Abbreviation

BEP	Best Efficiency Point
CFD	Computational Fluid Dynamics
DT	Draft Tube
FRM	Frozen Rotor model
GCI	Grid Convergence Index
GV	Guide Vane
LE	Leading edge

NPR   Negative pre-rotation: pre rotation in the opposite direction as the impeller

PHS   Pumped hydropower storage

PPR   Positive pre-rotation: pre rotation in the same direction as the impeller

PS   Suction side of the impeller

RANS   Reynolds-Averaged Navier Stokes

RMS   Root Mean Square

RP   Rainpower AS

RPT   Reversible Pump Turbine

SS   Suction side of the impeller

Indices

1   Position indication, high pressure side of the RPT[1]

2   Position indication, low pressure side of the RPT[1]

exp Experiment

i Direction

j Direction

m Projection on the meridional direction

u Projection on the circumferential direction

---

[1]This position is defined as the same, regardless the mode of operation

—————————— **Chapter I** ——————————

Introduction

1.1   Motivation

Human emissions are estimated to have caused approximately 1.0°C of global warming above pre-industrial levels. In order to stay within the 1.5°C degree ambition of the Paris agreement, global net anthropogenic CO2 emissions needs to be reduced to about 45% of the levels measured in 2010 by 2030 [1]. In order to be able to eventually reach the net zero goal, renewables must supply the majority of the electricity.

Intermittent renewables like solar- and wind power are on the rise as a consequence of the goal of reducing the global warming. Europe installed 15.4 GW wind power capacity during 2019 which was a 27% increase compared to 2018. The daily peak production was 102GW registered on 13th of march. However, a couple of days later the production was down to about 30GW [2] which is an example of the unsteady nature of wind power. Solar power added 100GW in 2018 and topped the list of installed renewable power capacity this year [3, p. 40]. Both wind- and solar power are examples of of intermittent renewables. It is important to stabilise the power grid in order for the end user to have a reliable source of energy and avoiding extreme levels of price volatility [4, 5]. Energy storage technologies offers support to the intermittent renewables and the power grid by extracting and releasing power from the grid when needed in order to stabilise it.

Energy storage is currently dominated by PHS which accounts for about 94% of the total storage capacity in 2018 [6]. PHS is proven to be an essential component for the modern and clean energy systems by storing energy for sustained periods. PHS works by extracting power from the grid and uses it to pump water from a lower reservoir to a higher reservoir in order to store the energy as potential energy. When there is need for this stored energy, it is converted back to electrical power through

a turbine when the water runs from the higher reservoir to the lower reservoir. PHS consists of either a separate pump and turbine or a single RPT. A single RPT is the dominant design for modern PHS [7].

Norway had 50% of the total installed hydropower storage in Europe in 2015, where most of it is used for production [8]. This large storage capacity can potentially be used to balance the the power grid in Europe. Most of the currently existing hydropower plants in Norway are designed for Francis turbines. Increased capacity of PHS can be achieved by modifying currently existing hydro power plants by replacing the turbine with a RPT. This task is currently being reviewed by HydroCen [9]. If a RPT is to replace a Francis turbine, the RPT will in pump mode most likely experience unwanted cavitation. Cavitation can be reduced or mitigated by adding a booster pump upstream of the RPT. A booster pump can potentially produce pre-rotation to the inlet of the RPT. How this effects the cavitation performance of a RPT in pump mode is going to be investigated in this thesis.

1.2 Objectives and limitations

The objective of this thesis is to investigate the cavitation performance of an existing RPT in pump mode of operation with pre-rotation using computational fluid dynamics (CFD). Steady-state multiphase simulations of the RPT in pump mode are performed at 3 different operating points relatively close to the best efficiency point (BEP). Pre-rotation is added to the inlet boundary based on a simplified rotation coming from an axial booster pump. This is done in order to examine effects of pre-rotation on the pressure and cavitation performance of the RPT. The pressure increase of the booster pump itself would add to the system is not considered in this thesis.

The computational domain and operation points has been limited in order to reduce computational time for this thesis. Numerical simulations were performed on a single passage of the guide vane (GV) and impeller in addition to the converging part of the draft tube (DT) after the bend. Due to the simple computational domain in combination with the numerical setup, secondary flows created by the bend in the DT is not investigated. This thesis is limited to the technical aspect of cavitation on a RPT in pump mode of operation. The RPTs Turbine mode of operation is not considered because cavitation is most likely to occur in pump mode. The economic aspect of the task of replacing a turbine with a RPT has also been disregarded.

1.3 Outline

This thesis consist of two theory parts: chapter 2 and 3 introduces the basic theory of turbomachinery and numerical simulations. It is important to have a solid theor-

etical foundation in order to be able to accurately simulate a problem using CFD, both with regards to the physical turbomachinery but also the CFD aspect.

Chapter 4 discusses the CFD setup used for multiphase simulations in this thesis. This includes the choice of computational domain, mesh, numerical setup in addition to mesh independence study at the different operating points.

Chapter 5 presents results from multiphase simulations without pre-rotation where the objective is to validate the CFD model using experimental data.

Chapter 6 provides the results from multiphase simulations with pre-rotation and the effects it has on the cavitation performance and pump curves for the RPT.

Chapter 7 and 8 discloses the final conclusion and proposes further work on the topic.

—————————— **Chapter II**——————————

Turbomachinery theory

■ It is important to have a solid theoretical foundation in order to be able to accurately simulate a problem using CFD. This chapter therefore covers the basic theory of hydromachinery most relevant for this thesis.

2.1   Reversible pump turbine (RPT)

RPTs are widely used in PSH stations [10]. A RPT is designed to be able to function as both a turbine and a pump which is usually referred to as RPT in pump- or turbine mode of operation. At what mode of operation a RPT is in dependents on the direction of rotation of the impeller. RPTs are highly flexible and are able to react to changes in the grid within minutes [11]. A RPTs impeller is designed mainly as a pump in order to be able to pump against the grater head that is in pump mode as seen in Figure 2.1.

For a RPT in pump mode, the Euler's pump equation is give by:

$$gH = \eta_h \left(u_1 c_{u1} - u_2 c_{u2} \right) \tag{2.1}$$

where indices 1 and 2 denote the high- and low pressure side of the RPT regardless of the mode of operation and g, H, η_h, u and c_u are the gravitational constant, head, hydraulic efficiency, circumferential velocity and the circumferential component of the absolute velocity according to Figure 2.2 respectively. Euler's turbomacinery equation gives an overview of how to design a pump in order to have the highest efficiency or head.
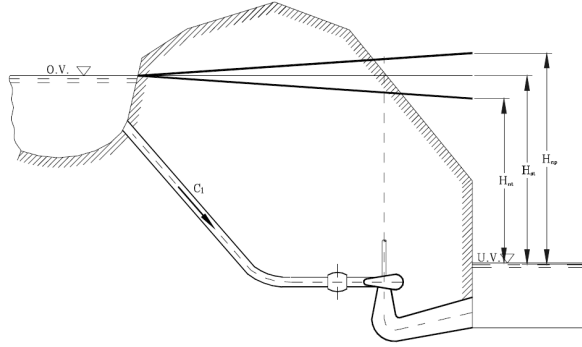
Figure 2.1: Difference in head for a RPT in pump- and turbine mode of operation
Collected from [12].

The head of an RPT is defined in Equation 2.2

$$H = \frac{p_1 - p_2}{\rho g} + \frac{c_1^2 - c_2^2}{2g} + (z_1 - z_2) \tag{2.2}$$

where p, and z is the static pressure and the height respectively. Velocities for a
RPT is defined from Figure 2.2. During the numerical simulations in this thesis,
gravitational model is not included. Therefore the the heights z was excluded from
Equation 2.2.

The hydraulic efficiency η_h in pump mode of operation is defied as:

$$\eta_h = \frac{P_h}{P_m} = \frac{gQH}{nT} \tag{2.3}$$

where P_h and P_m, Q and T is the hydraulic power, mechanical power, volumetric
discharge and torque on the impeller respectively. Contrary to the international
standard [13], this thesis does not consider "disk friction losses" and leakage losses
as hydraulic losses.

2.2 Dimensionless terms

Dimensionless numbers are used to compare one pump to another. A variety of
definitions are presented in the literature [12, 14, 15]. That is why this section is
based on the International Electrotechnical Commissions standards [13].

The specific speed n_s, is a dimensionless number that indicates what category the
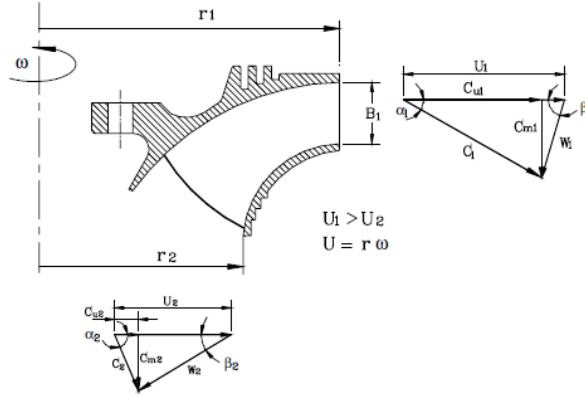
Figure 2.2: Velocity triangles for a RPT. Collected from [12].

RPT lies within.

$$n_s = \frac{nQ^{0.5}}{(gH)^{0.75}} \tag{2.4}$$

Discharge factor Q_{ED}, is a dimensionless mass flow rate and it is defined as:

$$Q_{ED} = \frac{Q}{D^2(gH)^{0.5}} \tag{2.5}$$

where Q, D and H is the volume flow, reference diameter and head respectively. The speed factor n_{ED} is defined as:

$$n_{ED} = \frac{nD}{(gH)^{0.5}} \tag{2.6}$$

2.3 Cavitation

Cavitation is problematic in hydromahinery mainly due to two different effects: pitting erosion and partial blockage of the impeller's passages [12, 14, 15]. Cavitation is the phenomena where water liquid reaches a region where the local absolute static pressure is below the liquid's vapor pressure $p < p_{va}$. When this is the case, the water turns into vapor and forms cavities in the fluid flow. If the cavitating zone is large, the head and efficiency of the RPT can be significantly reduced [14]. In a pump it is most common that cavitation occurs near the leading edge (LE) of the impeller. When the cavitation bubble is transported downstream to a region

with higher pressure, it collapses. In a pump, this is likely to happen close to the impeller blade. When the collapse of the cavitation bubble is occurring close to a physical surface, it causes a very large local pressure on the surface. This may lead to pitting erosion. If this is happening over longer periods, mechanical failure sight occur. The collapse of a cavitation bubble near a wall is illustrated in Figure 2.3.
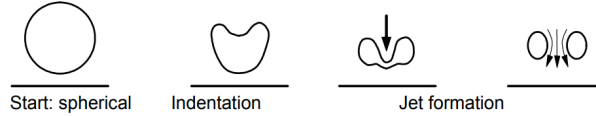
Figure 2.3: Collapse of a cavitation bubble near a physical wall. Collected from [14]
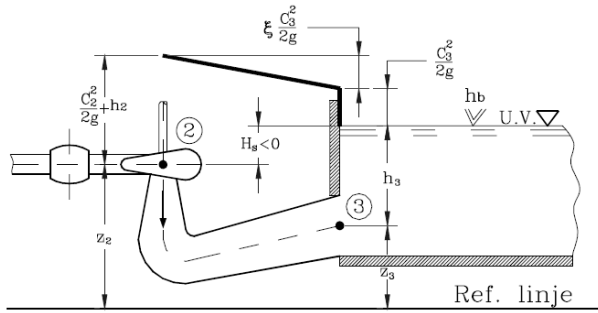
Figure 2.4: Submergence of a RPT. Collected from [12].

Net positive suction head ($NPSH$) is a measurement of cavitation conditions under which the hydro machine is operating. The available net positive suction head $NPSH_A$ is defined as the following:

$$NPSH_A = \frac{p_{tot,2} - p_{va}}{\rho g} = h_b - h_{va} - H_s \tag{2.7}$$

where the $p_{tot,2} = p_2 + \frac{1}{2}\rho c_2^2$ is total pressure at the low pressure side of the RPT, h_b is the barometric pressure, h_{va} is the vapor pressure and H_s is the submergence height which has a negative value when the RPT is located lower than the lower reservoir according to Figure 2.4. The required net positive suction head $NPSH_R$ is defined so that the turbomachine is not cavitating as long as $NPSH_A > NPSH_R$. An empirical formula for $NPSH_R$ is defined by:

$$NPSH_R = a\frac{c_{m2}^2}{2g} + b\frac{u_2^2}{2g} \tag{2.8}$$

where the velocities is according to Figure 2.2 and the coefficients a and b is determined empirically according to Table 2.1[12]. From this, it can be seen that a turbine has a lower $NPSH_R$ than a pump. This means that if a turbine $NPSH_A$ is close to the $NPSH_R$ is to be replaced with a RPT, the RPT is expected to experience cavitation due to $NPSH_A < NPSH_R$.

Table 2.1: Empirical data for the constants a and b when determining $NPSH_R$

Constant	Pump	Turbine
a	$1.6 < a < 2.0$	$1.05 < a < 1.15$
b	$0.2 < b < 0.25$	$0.05 < b < 0.15$

Thoma cavitation number

The Thoma cavitation number is a non-dimentional number based on the NPSH and the head of the pump, and is defined as the following

$$\sigma = \frac{NPSH_A}{H} \tag{2.9}$$

where H is the head. There are some different ways a sigma break curve can look as seen in Figure 2.5.

The inception cavitation is defined at σ_i where cavitation is first observed. The required Thoma number σ_R is defined as 1 % drop in efficiency due to cavitation in this thesis. Both σ_i and σ_R can be seen in Figure 2.5. From the definition of σ_R, it can be seen that in order for the RPT to avoid cavitation $\sigma > \sigma_R$ for all operating points. From Equation 2.7 and 2.9 it can be observed that the higher the maximum σ_R is for a RPT, the required total inlet pressure must be higher as well in order to assure that no cavitation is occurring.
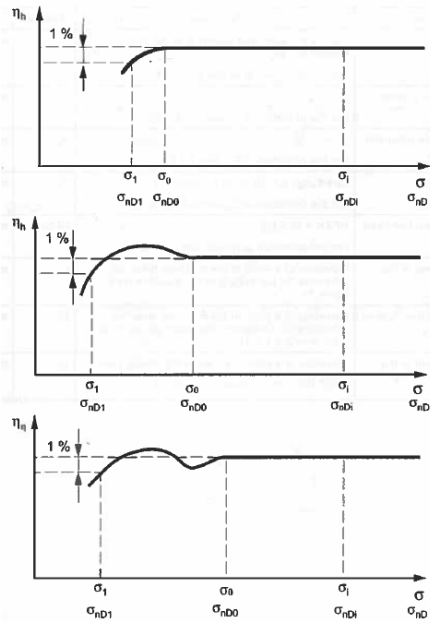
Figure 2.5: Typical sigma beak curves. Collected from [13]

When combining Equation 2.7, 2.9 and 2.2 and solve for the total inlet pressure,we get:

$$p_{tot,2} = p_{va} + \rho g \sigma H \tag{2.10}$$

where $p_{tot,2}$ is the total inlet pressure. This is used as inlet condition in chapter 5.

Cavitation on a RPT in pump mode

If cavitation is present for a well designed RPT in pump mode of operation, this usually occurs near the inlet of the impeller where the static pressure p is smallest.

In order to mitigate cavitation, the local pressure needs to be sufficiently high in the entire pump. There are several ways of increasing σ. A common solution is to install the pump physically at a lower level compared to the lower reservoir. Another way of increasing the local pressure is to add an a booster pump in series upstream of the pump where the cavitation is occuring.
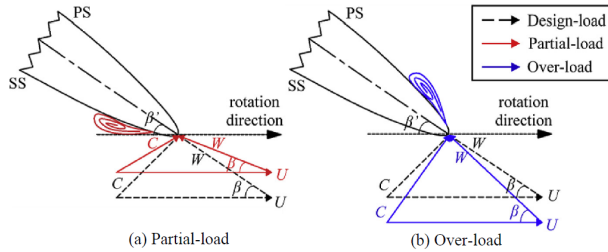
Figure 2.6: Velocity triangles on the leading edge of the impeller for part load and overload conditions. Collected from [10]

2.4 Booster pump and pre-rotation

If a pump is experiencing cavitation under normal operating conditions, a booster pump can be installed upstream in order to increase the inlet pressure [14]. When operating in series, both the RPT in pump mode and the booster pump delivers the same flow rates. The combined characteristics are therefore found by adding the heads of the RPT in pump mode and the booster pump. In other words, installing a booster pump increases the head of the system.

A general approach when designing a RPT in pump mode is to assume zero pre-rotation at the inlet and a uniform axial velocity profile. Zero pre-rotation means that the circumferential component of the absolute velocity at the inlet C_{u2} is zero. The impeller is designed with a BEP where the relative inflow angle (β) and the inlet impeller blade angle (β') is equal. The impeller can not change the blade angle so when the flow rates change from BEP then $\beta \neq \beta'$ as seen in Figure 2.6. This reduces the efficiency of the RPT and increases the possibility of separation near the LE of the impeller. The relative inlet flow angle can be regulated with pre-rotation in order to align it with the impeller blade angle in order to reduce the negative effects of off-design operation. According to the Euler Equation 2.1 it can be observed that any positive pre-rotation (PPR) in the same direction of rotation as the impeller will decrease the head, and any negative pre-rotation (NPR) increases power and head [14, p. 661]. Pre-rotation for a pump has been investigated using inlet guide vanes by Liu et al. [16] and Ahmed et al. [17]. The papers shows that pre-rotation can broaden the efficient operation range due by reducing the difference between β and β'. A masters thesis from NTNU by Larsen [18], studied the same RPT as discussed in this thesis with pre-rotation. No increase in efficiency was found, but NPR increased the head and the PPR decreased the head as predicted from the theory. How pre-rotation effected cavitation characteristics was not investigated in that thesis.

In this thesis, it is assumed that the booster pump is an axial pump. An axial forced vortex is observed on these types of pumps. This vortex is created when a uniform axial flow is superimposed with a forced vortex [19]. In a forced vortex, the angular velocity of the fluid in constant which means that the fluid is revolving as a solid body. This is used as the inlet velocity profile for the RPT with pre-rotation for the entire DT and is described in detail in chapter 6.

Chapter III

Numerical simulation theory

■ Numerical simulation can be used when the flow is too complex to calculate analytically. This is an approximation of the real solution and it is therefore important to keep tack of the errors of the simulations. In this chapter, the theory of numerical simulations most relevant to the problem at hand will be discussed.

The two fundamental approaches to analyse fluid dynamics problems are experimentation and calculation [15, p. 880]. The experimental approach consists of building a scale model and perform tests on it, which is economically expensive and time consuming. The calculation method involves solving partial differential equations either analytically or numerically. Real flows can generally not be solved analytically [14, p. 429] and this is where numerical approach is useful. Numerical simulation is the chosen method for this thesis.

CFD works by transferring the governing equations into a computation domain called a mesh. The mesh is consisting of a finite number of volumes, called cells. The governing equation needs to be discretised and solved for each cell in the mesh. Ansys CFX solves the governing equation by using the finite element method. This means that the geometry which is wanted to be simulated, must be reduced to finite number of elements. In this thesis, we are interested in solving the problem in three dimensions and will therefore need a finite number of small volumes.

The partial differential equations in question are described in the following section.

3.1 Governing equations in fluid dynamics

The governing equations in this section is based on Viscous fluid flow of White[20] and a paper from Ytrehus [21]. It is important to have an understanding of some of the most important equations that can be solved in a CFD software. After a simulation, the same equations can be used in order to coarsely check whether the simulation seems physical. The three basic conservation laws in fluid dynamics are:

1. Conservation of mass (continuity)

2. Conservation of momentum (Newton's 2nd law)

3. Conservation of energy (first law of thermodynamics)

Conservation of energy will not be discussed further because in this thesis, as the fluid was considered to be isothermal. The following equations will use tensor notation.

Continuity equation

The continuity equation is the conservation of mass. The general continuity equation:

$$\frac{\partial \rho}{\partial t} + \frac{\partial}{\partial x_j}(\rho c_j) = 0 \tag{3.1}$$

where ρ is the fluid density, t it time and x_j and c_j is the distance and velocity in j-direction respectively. Incompressible fluids use the simplified continuity equation found in Equation 3.2.

$$\frac{\partial c_j}{\partial x_j} = 0 \tag{3.2}$$

It is common to assume that water is incompressible and use Equation 3.2.

Navier-Stokes equation

The Navier-Stokes equation is derived from conservation of momentum. The Navier stokes equation for a Newtonian fluid:

$$\rho \frac{Dc_i}{Dt} = -\frac{\partial p}{\partial x_i} + \frac{\partial}{\partial x_j}\left[\mu\left(\frac{\partial c_i}{\partial x_j} + \frac{\partial c_j}{\partial x_i} - \frac{2}{3}\delta_{ij}\frac{\partial c_k}{\partial x_k}\right)\right] + \rho f_i \tag{3.3}$$

where p, μ and f is the pressure, static viscosity and the external body force respectively. The incompressible version of the Navier-Stokes equation:

$$\rho \frac{Dc_i}{Dt} = -\frac{\partial p}{\partial x_i} + \mu \nabla^2 u_i + \rho f_i \qquad (3.4)$$

3.2 Mesh

The accuracy of the CFD solution is governed by the number of cells in a mesh [22]. Even if the numerical setup were to be perfect, a bad mesh will provide bad results. A finer mesh is usually more computational expensive and an optimal mesh is therefore not uniform in order to have finer cell sizes in regions of high gradients and a coarser cells in low gradient regions.

There are two different types of mesh. The structured mesh and unstructured mesh [15, p.884]. Unstructured volumetric meshes make it possible to mach the boundary shape of complex geometry. Structured volumetric meshes consists of cells with 6 sides, as hexagons. In structured meshes, the hexagons can be skewed. The main advantage of structured mesh is the reduction in number of cells compared to unstructured mesh [15]. Regardless of the type of mesh, the quality of it is critical for accurate CFD solutions.

Measures of mesh quality

There are numerous ways of evaluating mesh quality, but the following three are used during this thesis. **Orthogonality Angle** is the area averaged of $90(degree) - acos(n \cdot s)$ according to Figure 3.1.
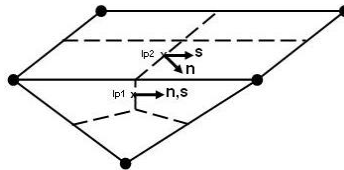
Figure 3.1: Orthogonality Angle. Collected from [23]

Aspect ratio is the largest ratio of maximum to minimum areas for elements adjacent to a node [23]. **Expansion factor** is the largest ratio of largest to smallest sector volumes for each cell in the mesh.

A good mesh quality is important in order to control the discretisation error.

(a) Expansion ratio. Collected from [23]   (b) Aspect ratio. Collected from [23]
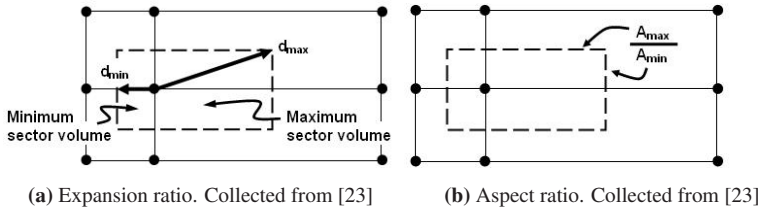
Figure 3.2: Explanations for measures of mesh quality

3.3   Multiphase

Cavitation is a multiphase problem because both the liquid and the gas phase of water is present in the flow. When simulating a cavitation problem, it is recommended to initialise it from a converged single phase steady-state simulation. The region where cavitation is expected to be formed is near the LE of the impeller, and the mesh is therefore fine in this region.

According to [14, p. 470], the three main ways of simulating cavitation is the following:

1. Calculation of the cavity length without coupling the main flow.

2. Evaporation at constant enthalpy.

3. Mixing of gas and liquid phase. The two phases is treated as a homogeneous.

The focus will be the on the latter method. In this case the Rayleigh–Plesset model [24] for the phase change interface is used. This a simple model that neglects mass and heat transfer across the interface [25].

When making a sigma break curve in CFD, the rotational speed and displacement is kept constant. The simulation is first established as a single phase simulation with high inlet pressure. Simulations with progressively lower total inlet pressure are then conducted with interphase mass transfer enabled between the two different phases. This is performed until the drop in efficiency occurs.

3.4   Boundary conditions

For pumps and turbines, the recommended boundary conditions are total pressure inlet and mass flow outlet assuming that the machine is drawing fluid directly from a static reservoir. The specification of mass flow inlet may be more robust [26]. An

alternative is velocity inlet and static pressure outlet. This is a very stable boundary condition and is better to be used when explicit control of inlet velocity is required.

3.5   Turbulence modeling

Most engineering flows encounters turbulence [22] and RPTs are no exemption. The Navier-Stokes equation includes turbulence, but in order to simulate this numerically, the mesh must be fine enough in order to solve the smallest eddies. This method is not feasible for the simulation in question in this thesis. Using the Reynolds averaged Navier Stokes equation (RANS) with a suitable turbulence model which describes the distribution of the Reynolds stresses in the fluid [14, p.434]. For turbulence induced cavitation, Ansys suggests using detached eddy simulation turbulence model [26]. This is not considered in this thesis. The standard $k - \epsilon$ model is a two equation turbulence model which uses two transport equations to determine. This turbulence model is widely used in the industry due to its stable performance. It uses scalable wall function in order to model the flow near boundaries.

3.6   Boundary layer modeling

The no-slip condition at the walls cause large velocity gradients near the wall, inside the boundary layer. This is an effect of the viscosity of the fluid. Normalised values for the velocity and distance from the wall are commonly used and discussed in these cases. The Nondimensional wall distance is:

$$y^+ = \frac{\rho w_\tau y}{\mu} \tag{3.5}$$

where the nondimensional velocity is $w^+ = \frac{w}{w_\tau}$, the shear velocity is $w_\tau = \sqrt{\frac{\tau_w}{\rho}}$, τ_w is the shear stress, w is the relative velocity and y is the distance from the wall.

For high Reynolds's numbers, the wall functions in the $k - \epsilon$ turbulence model is used to resolve the viscous sublayer as seen in Figure 3.3. The log layer needs to be solved and the near-wall mesh points should therefore be positioned in the region $30 < y^+ < 500$ [22], in no case $y^+ < 11$ [14] and contain at least 10 nodes within the boundary layer [26]. Turbulence models using wall functions does not require as fine mesh as turbulence models that need to solve the viscous sublayer directly.

3.7   Interface models

In order to be able to simulate the difference between a rotating- and a stationary domain, a model needs to be applied in the intersection between these areas. This is called a rotor stator interaction. For a steady state simulation in CFX, this can be
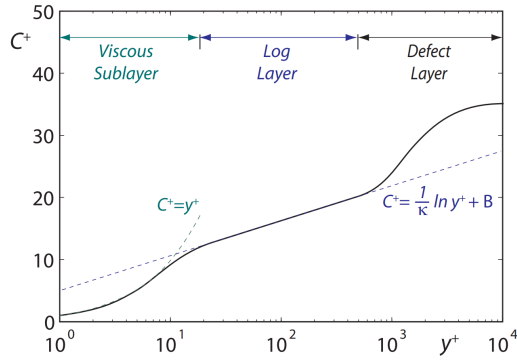
Figure 3.3: Typical turbulent boundary layer where $w^+ = C^+$. Collected from [27]

done using either *Frozen Rotor model* (FRM) or *Mixing-Plane model* (MPM). FRM changes the frame of reference from one component to the next while maintaining the relative position. This is usually used for components with approximately the same pitch ratio [26]. MPM circumferentially averages the fluxes in bands and sends it to the downstream component. The circumferential averaging makes this model good for large pitch ratios and it is a relatively fast interface model. This model is not suitable for significant wake interactions like for example the wake [26] from the impeller on the GV for a pump.

Chapter IV

CFD setup

■ This chapter describes the CFD setup that was used to provide the CFD cavitation results for the RPT in question. This includes the choice of computational domain, mesh and numerical setup in addition to a mesh independence study at the different operating points.

The geometry and experimental cavitation data at different operating points used in this masters thesis was provided by Rainpower AS (RP). The geometry consisted of DT, impeller, GV, stay vanes and spiral casing. In order to use this geometry, the author agreed that no information that can lead to the reproduction of the RPT should to be published. All results are therefore normalised.

Multiphase simulations was performed at the three different operating points as described in Table 4.1. These were chosen based on the limited experimental cavitation curves available.

Table 4.1: Operating points

Name of operating point	Q/Q_{BEP}	$\alpha_{GV}/\alpha_{GV,BEP}$
Low Q	0.8408	0.7839
BEP	1	1
High Q	1.1293	1.0635

4.1   Computational domain

The RPT investigated in this thesis has a specific speed of $n_s = 0.58$ in pump mode and consists of 9 impeller blades, 26 guide vanes, 26 stay vanes.

Multiphase simulations are computationally expensive. It was therefore decided to reduce the computational domain of the RPT as much as possible. At an early stage multiphase CFD simulations of one impeller passage was performed in order to check if it was realistic to perform more complex multiphase simulations with a larger computational domain later on. This was successful and is described in greater detail in Appendix A. In order to get an as accurate simulation as possible, the entire geometry should have been simulated. From the multiphase simulations of a single passage, it became apparent that simulating the entire RPT was unrealistic with respect to the available computing resources. An attempt of simulating all passages for the impeller and GV with the full geometry of the DT was unsuccessful. This was most likely due to separation in the DT in combination with the FRM interface resulted with two of the impeller passages was stalled. FRM remains the relative position between the DT and the impeller. The two stalled impeller passages were considered to be unphysical as the large turbulence regions in the real world would be more evenly distributed between all the impeller regions due to the rotor stator interaction of the impeller, DT domains.

Figure 4.1: Computational domain

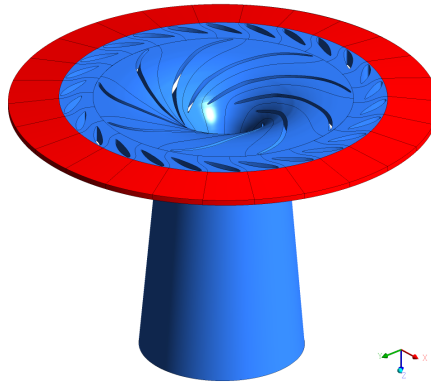The final computational domain used during this thesis was one impeller passage, one GV passage and a "short DT". The short DT is defined as the portion of the DT downstream of the bend. The pitch ratio between one impeller passage and the short DT is large and the pitch ratio from an impeller to a GV is significant. Based on these larger pitch ratios, the MPM interface model was chosen. Asymmetrical

flow from the DT would not be captured by this interface model due to the circumferential averaging. This was another reason to use the short DT. CFD simulations with this computational domain, struggled with convergence due to back-flow at the outlet. The outlet boundary was set to opening but the results was only marginal improved. As a solution, it was decided to extend the outlet with a converging section which has $1/3$ of the height and 3 times the length compared to the height at the outlet of the GVs. This converging section is marked in red in Figure 4.1 increased the radial velocity near the outlet of the simulation and thus reduces the back-flow. The converging section was set to full-slip wall boundary condition in order to influence the pressure loss as little as possible. The computational domain with graphical instancing for the impellers and GVs can be seen in Figure 4.1. It should be noted that the high pressure side of the RPT denoted 1 was set to the intersection between the GVs and the converging section in order to reduce influence of the converging section has on the results.

4.2 Mesh

The mesh quality has a direct impact on the accuracy of a CFD simulation [15]. Effort was made into a variety of meshes in order to find a balance between accuracy and computational times. The mesh was designed for a $k-\epsilon$ turbulence model with scalable wall function. The first node y^+ was aimed to be within the desired range, the number of nodes within the boundary layer was 10 as described in Table 4.2 and a growth rate of $1.5 - 2$.
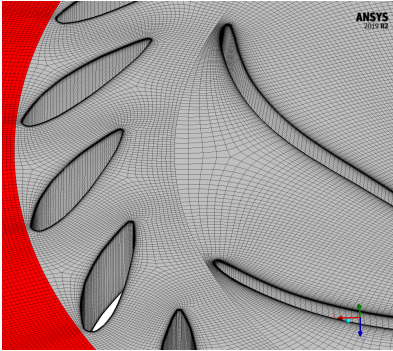
Figure 4.2: Detailed surface mesh at BEP, medium mesh
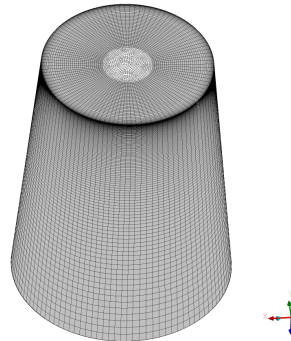
Figure 4.3: Surface mesh of the short DT, medium mesh

The software used for CFD analysis was Ansys 19.4. The Impeller and GV passage were meshed using *Turbogrid* which provides a structured hexahedral mesh. This program uses curve files as input which consists of three dimensional points

describing the hub, shroud and the blade geometry. From these files, *Turbogrid* determines an appropriate mesh based on a couple user inputs. The detailed surface mesh for the medium mesh size at BEP is seen in Figure 4.2. The short DT was meshed using *Ansys Meshing*. The hexahedral mesh was produced with the use of *MultiZone*. Effort was made into get as smooth transition as possible between the different domains in the simulation. This resulted in a lot better transition between the domains and provided better convergence.

There is a difference in the GV meshes at the different operating points due to the different GV angle α_{GV} and the ratio can be seen in Table 4.1. The mesh sizes used for mesh independence study is found in Table 4.2, 4.3 and 4.4.

Table 4.2: Mesh sizes for low Q

Number of cells	Extra Fine mesh (N_0)	Fine mesh (N_1)	Medium mesh (N_2)
The draft tube	2,490,800	1,243,840	560,706
One impeller passage	4,925,184	2,446,092	1,190,574
One guide vane passage	1,083,993	546,720	268268
Total number of cells	**8, 499, 977**	**4, 236, 652**	**2, 019, 548**

Table 4.3: Mesh sizes for BEP

Number of cells	Fine mesh (N_1)	Medium mesh (N_2)	Coarse mesh (N_3)
The draft tube	1,243,840	560,706	271,016
One impeller passage	2,446,092	1,190,574	592,812
One guide vane passage	871,536	365,150	180,766
Total number of cells	**4, 561, 468**	**2, 116, 430**	**1, 044, 594**

Table 4.4: Mesh sizes for high Q

Number of cells	Fine mesh (N_1)	Medium mesh (N_2)	Coarse mesh (N_3)
The draft tube	1,243,840	560,706	271,016
One impeller passage	2,446,092	1,190,574	592,812
One guide vane passage	838,438	425,651	165,624
Total number of cells	**4, 528, 370**	**2, 176, 931**	**1, 020, 608**

Mesh quality

The mesh quality of the meshes chosen in the previous section is considered here. The quality of the mesh was based on the following quality criterion that follows the general advise from Ansys [23]:

- Orthogonality Angle > 20°

- Aspect ratio < 100

- Expansion factor < 20

where the different criterion are described in section 3.2.

The coarse meshes used for mesh independence study, had the "worst" mesh statistics. The coarse mesh designed for BEP has a minimum orthogonality angle of 49.0° and a maximum expansion factor of 6. Both of these are considered to be very good. The maximum aspect ratio for the mesh is 184. The high aspect ratio regions are located close to the hub and shroud in the converging section and in the impeller domain close to the hub and shroud, midway in the passage, away from the blade near the trailing edge (TE). The percentage of bad cells was less than 1% and this was therefore deemed good for the mesh independence study. The more refined meshes has considerably better mesh statistics due to the increased number of cells without reduction in the cells inside the boundary layer.

4.3 Numerical setup

Table 4.5: Numerical multiphase setup in Ansys CFX

Parameter	Description
Solver	Ansys CFX 19.4
Analysis type	RANS, Steady-state
Interface	Mixing-Plane model (MPM)
Advection scheme	High resolution
Turbulence scheme	First order
Turbulence model	standard $k - \epsilon$ with scalable wall function
Physical timescale	$\sim 0.1n^{-1}$
Mesh type	structured, hexahedral
Mesh	Mesh sizes according to Table 4.3,4.4 and 4.2
First node y^+ statistics	Draft tube average: 59 - 82
	Impeller average: 50 - 61
	Guide vane average: 52 - 53
Boundary conditions	Inlet: total pressure according to Equation 2.10,
	5% turbulence intensity
	liquid water fraction: 1
	Outlet: bulk mass flow rate
	Walls: no slip, smooth walls [1]
Cavitation model	Rayleigh Plesset
Saturation pressure P_{va}	3782 (Pa)
Temperature	28 (°C) [2]
Convergence criteria	RMS of continuity, momentum, pressure and
	turbulence quantities $< 10^{-6}$
Iterations per run	< 1500 [3]

p_{va} is on the absolute scale and compared to the absolute static pressure in order to determine if parts of the fluid is at risk of cavitation. The reference pressure was therefore set to $p_{ref} = 0(Pa)$ in order to get the static pressure to be the absolute static pressure: $p = p_{abs}$.

The **inlet boundary condition** is very important during the multiphase simulations because it determines p in conjunction with p_{va}, to what degree cavitation is occurring. This boundary conditions was set to total pressure corresponding to σ of the

---

[1]Exception: free-slip condition for the converging extension of the GV.

[2]This temperature was used to set the correct fluid properties using linear interpolation between 25(°C) and 30(°C), except P_{va} which was found directly.

[3]The initial simulation had $800 <$ iterations.

experimental data and the H of initial single phase simulation using Equation 2.10. Additional points was added in comparison to the experiments in order to get a smoother curve for the CFD simulations.

The first node $y+$ values was in in the range 1 - 256 where the lowest y^+ was located at the mid-span, at the high pressure side of the impeller and is not considered a critical region. For the $k - \epsilon$ turbulence model with wall functions, this should be above 11 as discussed in chapter 3. However, buy using the scalable wall function this is not an issue [26]. The meshes are deemed good according to the $y+$ requirement of the turbulence model.

4.4 Mesh independence study

Estimation of discretisation error was done according to the procedure described by Celic et al. [28]. In order to provide an estimation for the discretisation error, 1500 iterations of the three operating points described in Table 4.1 was performed without multiphase simulation and without pre-rotation. The different mesh sizes for the different operating points can be found in section 4.2. The monitored average root mean square (RMS) did not change after about 800 iterations and all monitored quantities like hydraulic efficiency, Thoma cavitation number and head did not change significantly as the number of iterations passed about 300.

The equations in this section does not use tensor notation. The mesh size is defined as the following:

$$h = \left(\frac{1}{N} \sum_{i=1}^{N} (\Delta V_i) \right)^{1/3} \tag{4.1}$$

where ΔV_i is the volume of the ith cell and N is the total number of cells used for the computations. The refinement factor $r_{ij} = h_i/h_j$, should preferably be grater than 1.3 based on experience [28]. The mesh refinement factor for the meshes in this thesis is just below 1.3. This was considered to be close enough to 1.3 because 1.3 is only based on experience. The error from one mesh to another: $\varepsilon_{ij} = \phi_i - \phi_j$. The apparent order p of the method, was found using fixed point iteration and the formula $p = \frac{1}{ln(r_{21})} \left| ln |\varepsilon_{32}/\varepsilon_{21}| + ln \left(\frac{r_{21}^p - sgn(\varepsilon_{32}/\varepsilon_{21})}{r_{21}^p - sgn(\varepsilon_{32}/\varepsilon_{21})} \right) \right|$. The extrapolated values defined as $\phi_{ext}^{ij} = (r_{ij}^p \phi_j - \phi_i)/(r_{ij}^p - 1)$. The approximated relative error: $e_a^{ij} = \left| \frac{\phi_j - \phi_i}{\phi_j} \right|$. The extrapolated relative error: $e_a^{ij} = \left| \frac{\phi_{ext}^{ij} - \phi_j}{\phi_{ext}^{ij}} \right|$. The grid convergence index was defined as $GCI^{ij} = \frac{1.25 e_a^{ij}}{r_{ij}^p - 1}$.

According to Table 4.6, the maximum discretisation error estimation using the Grid convergence index (GCI) was 0.996% for the fine mesh and 1.33% for the medium

Table 4.6: Mesh independence BEP

Parameter	$\phi = \eta_h$	$\phi = H$	$\phi = T$
N_1	4.561.468	4.561.468	4.561.468
N_2	2.116.430	2.116.430	2.116.430
N_3	1.044.594	1.044.594	1.044.594
r_{21}	1.29	1.29	1.29
r_{32}	1.27	1.27	1.27
p	4.679	2.485	1.120
$e_a^{21}\%$	0.109	0.374	0.264
$e_{ext}^{21}\%$	0.047	0.419	0.790
$GCI_{fine}^{21}\%$	0.059	0.526	0.996
$GCI_{med}^{32}\%$	0.196	0.997	1.330

Table 4.7: Mesh independence High Q

Parameter	$\phi = \eta_h$	$\phi = H$	$\phi = T$
N_1	4,528,370	4,528,370	4,528,370
N_2	2,176,931	2,176,931	2,176,931
N_3	1,020,608	1,020,608	1,020,608
r_{21}	1.28	1.28	1.28
r_{32}	1.29	1.29	1.29
p	9.472	0.640	8.388
$e_a^{21}\%$	0.028	0.408	0.380
$e_{ext}^{21}\%$	0.003	2.354	0.056
$GCI_{fine}^{21}\%$	0.004	3.014	0.070
$GCI_{med}^{32}\%$	0.039	2.588	0.009

Table 4.8: Mesh independence Low Q

Parameter	$\phi = \eta_h$	$\phi = H$	$\phi = T$
N_0	8,499,977	8,499,977	8,499,977
N_1	4,236,652	4,236,652	4,236,652
N_2	2,019,548	2,019,548	2,019,548
r_{10}	1.26	1.26	1.26
r_{21}	1.28	1.28	1.28
p	3.137	0.750	0.533
$e_a^{10}(\%)$	0.037	0.581	0.544
$e_{ext}^{10}(\%)$	0.035	2.967	3.966
$GCI_{X-fine}^{10}(\%)$	0.043	3.822	5.163
$GCI_{fine}^{21}(\%)$	0.090	4.575	5.874

mesh at BEP. The increase in computational time from medium to fine mesh was not considered to be worth the 0.334 percentage point decrease in discretisation error. Thus, the medium mesh was chosen for simulations at BEP. As seen in Table 4.7, the GCI for the medium mesh is 2.588%. This is higher than for BEP, but this is as expected due to a slightly more complex flow pattern at off-design operating conditions. This discretisation error is deemed sufficiently good for the medium mesh and it is chosen for the high Q operating point. The low Q operating point had an unacceptable high GCI with one order of magnitude higher GCI than the other operating points. It was therefore decided to perform mesh independence study on the medium to extra fine mesh. Table 4.2 describes the number of cells in the different meshes for this operating point and Table 4.8 shows the mesh independence. From the last table, the maximum GCI for the low Q operating point with the fine mesh is 5.874% which is acceptable and the fine mesh is therefor chosen for this operating point.

To summarise, the medium mesh was chosen for both BEP and low Q operation conditions. The fine mesh was chosen for the low Q operating condition. The highest GCI values for the chosen meshes is 5.874% which was considered to be

sufficient for the simulations with cavitation.

--------- Chapter V ---------

Multiphase simulation validation without pre-rotation

∎ In this chapter, multiphase simulations will be compared to the experimental data at different operating points without pre-rotation.

The simulations performed in this chapter used the CFD setup discussed in chapter 4 with the medium mesh for BEP and high Q operating point. The low Q operating point uses the fine mesh as discussed in section 4.4. In order to keep the confidentiality agreement between RP and the author, it was decided to use normalised values. The normalised hydraulic efficiency $\overline{\eta}_h$ was defined as:

$$\overline{\eta}_h = \frac{\eta_h}{\eta_{h,\text{best efficiency}}} \tag{5.1}$$

where $\eta_{h,\text{best efficiency}}$ was the highest hydraulic efficiency for the simulation run or the experimental series. The normalised Thoma cavitation number $\overline{\sigma}$ is defined as:

$$\overline{\sigma} = \frac{\sigma}{\sigma_{\text{defined constant value}}} \tag{5.2}$$

where $\sigma_{\text{defined constant value}}$ is the same constant value for all the simulations. The different simulations $\overline{\sigma}$ can therefore be directly compared to each other.

5.1   Sigma break curves without pre-rotation

A slightly different definition of $\overline{\sigma}_h$ than described in Equation 5.1 is used to provide the sigma break curves. All simulations are divided by the highest efficiency without multiphase enabled and the experiments are divided by the max-

imum efficiency for the operating point. This was done in order to be able to compare the sigma break curves in more accurate way with respect to the $\overline{\sigma}$ values.

Low Q cavitation simulation

The max GCI for this operating point for the medium mesh was found to be 48%. This was unacceptably high, and it was therefore decided to choose the fine mesh for this operating point which had a maximum $GCI = 5.874\%$.
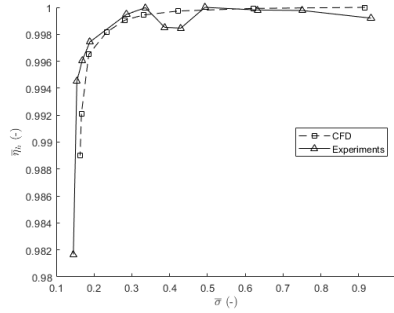

Figure 5.1: Sigma beak curve at low Q ($Q/Q_{BEP} = 0.8408$), no pre-rotation

The required sigma value $\overline{\sigma}_R$ for this operation point is $\overline{\sigma}_R = 0.164$ without pre-rotation and $\overline{\sigma}_R = 0.151$ for the experiments. The CFD simulation has in this case 8.6% higher $\overline{\sigma}_R$ compared to the experiments.

BEP cavitation simulation

A operation point with GV angle $\alpha_{GV} = 23.6$ (degree) close to the BEP of the RPT was simulated using the CFD setup discussed in chapter 4. The result is compared to experimental data and the single frame of reference simulation of the impeller only as discussed in Appendix A.

The required sigma value $\overline{\sigma}_R$ for this operation point is $\overline{\sigma}_R = 0.244$ without pre-rotation and $\overline{\sigma}_R = 0.209$ for the experiments. The CFD simulation has in this case 16.7% higher $\overline{\sigma}_R$ compared to the experiments. More CFD simulations should have been performed around the 1% drop in efficiency for more accurate $\overline{\sigma}_R$ and this might contribute to the high difference between the simulations and experiments.

High Q cavitation simulation

For this operation point, $\overline{\sigma}_R = 0.441$ without pre-rotation and $\overline{\sigma}_R = 0.412$ for the experiments. The CFD simulation has in this case 7.0% higher $\overline{\sigma}_R$ compared to the
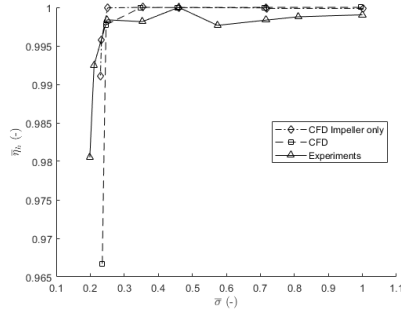
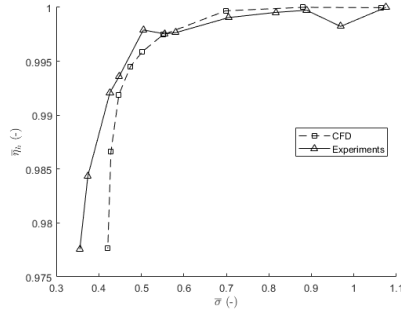**Figure 5.2:** Sigma beak curve at BEP, no pre-rotation

Figure 5.3: Sigma beak curve at high Q ($Q/Q_{BEP} = 1.1293$), no pre-rotation

experiments.

5.2 Discussion of multiphase simulations without pre-rotation

The errors in the experiments are unknown. However, the experiments are the average results and therefore will primarily systematic errors effect it. Care should be taken when comparing the CFD simulations to the experiments due to the unknowns in the experiments in addition to the CFD simulations.

The simulated sigma break curves shown in Figure 5.1, 5.2 and 5.3 seems to correlate well with the experimental data. The CFD simulations slightly over predict $\overline{\sigma}_R$ with an average of 10.8% compared to the experimental data. In other words: $\overline{\sigma}_R$ is a higher for the CFD simulations compared to the experiments.
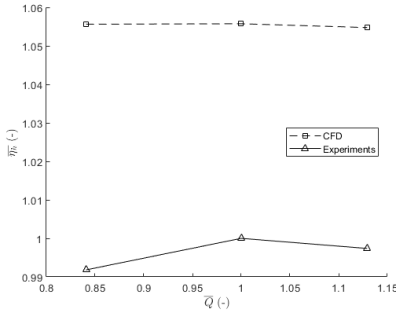
Figure 5.4: $\overline{Q} - \overline{\eta_h}$ curves without pre-rotation
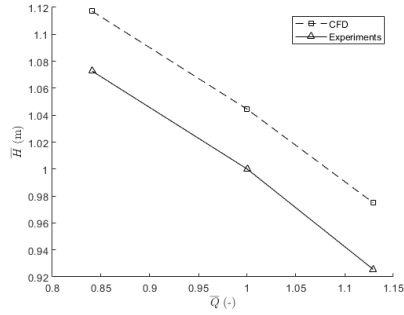
Figure 5.5: $\overline{Q} - \overline{H}$ curves without pre-rotation

From Figure 5.1, 5.2 and 5.3 it can be seen that the highest $\overline{\sigma}$ values are found for the high Q case. This indicates that for higher volumetric displacements cavitation is more likely to occur than in lower volumetric displacement cases.

With regards to to cavitation from chapter 5, it is seen that the highest Thoma number is occurring for the high Q operation condition.

The difference in the pump performance curves between the CFD simulations and the experiments in Figure 5.4 and 5.5 may be caused by the reduced computational domain. The reduced computational domain does not take losses the bend in the DT, SV and SC into account as it is neither simulated nor compensated for.

The CFD model is performing sufficiently good compared to experimental data and this model will be used to simulate pre-rotation in the next chapter.

———————————————— **Chapter VI**————————————————

Multiphase simulation results with pre-rotation

◼ If an axial booster pump is installed upstream of the RPT in pump mode, it might produce pre-rotation at the inlet of the RPT. This chapter evaluates the effect pre-rotation has on the pump performance curves and the sigma break curves using the validated CFD model of the RPT in question at different operating points.

6.1   CFD setup for the simulations with pre-rotation

The CFD setup for the simulations with pre-rotation uses the setup as described in chapter 4, but with two important changes:

- The inlet boundary condition was changed to velocity in order to create an accurate velocity profile to take pre-rotation into account. The inlet velocity profile was set as described in section 6.2.

- The outlet was set to static pressure.

This change in boundary conditions was done in order to get full control of the inlet velocity profile. It was not longer possible to calculate the exact outlet static pressure according to the desired σ without an initial guess and adjustments due to the pressure rise over the pump changes at different operating conditions as seen in Figure 5.5. The target σ values was about the same as in the simulations without pre-rotation. This pre-rotaion's primary task is to model the vorticity created by a booster pump in series and upstream of the RPT in pump mode as discussed in chapter 2.

Four different pre-rotations was simulated for each operating point as described in Table 4.1. This pre-rotation was set as a maximum angle between the uniform axial inflow and the circumferential velocity component with a velocity profile as described in section 6.2. The maximum angles was set to -40°, -20°, 20° and 40° where the negative value indicates negative pre-rotation (NPR) and the positive values indicates positive pre-rotation (PPR) in the same direction as the impeller blade.

6.2   Determining the inlet velocity profile of the short draft tube (DT)

The goal of this section is to quantitatively determine a reasonable inlet velocity profile for the short DT seen in Figure 4.3. In order to provide a reasonably inlet condition which mimics a real flow from an axial booster pump, the entire DT was simulated without multiphase. From this simulation, a reasonable velocity profile for pre-rotation at the inlet of the short DT is determined quantitatively. It is assumed that the booster pump is an axial pump, and therefore a forced vortex was superimposed with a uniform axial velocity profile as described in section 2.4, on the inlet of the full DT. This can be seen in Figure 6.1.

(a) Axial velocity profile   **(b)** Circumferential velocity profile
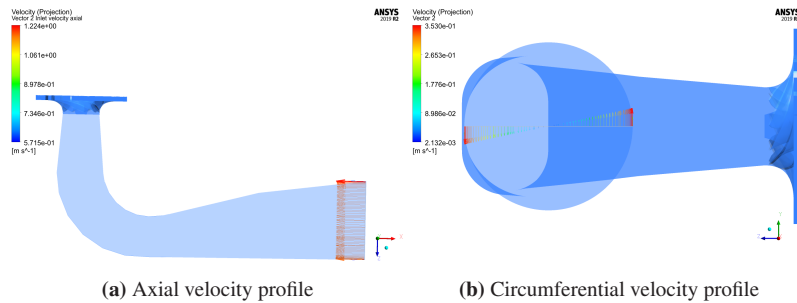
Figure 6.1: Inlet velocity profiles for the full DT

The inlet was set to a forced vortex which is a coarse simplification of the pre-rotation of a booster pump upstream of the RPT. The amount of pre-rotation was set arbitrary. This is because it is how the vortex evolves through the bend of the DT that is of interest.

Separation occurs due to the ~ 90 (degree) bend in the DT despite using the $k - \epsilon$ turbulence model which captures separation poorly [14] as seen at the inside of the bend in Figure 6.2. Due to the irregular flow right after the bend, the plane used to determine the velocity profile to be used in the rest of the simulations is located

Figure 6.2: The velocity contour in DT for the DT simulation

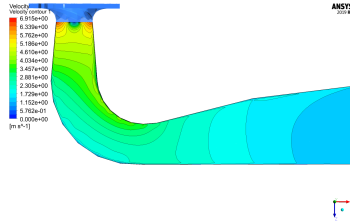about mid way between the end of the bend in DT and the outlet of the DT.

(a) Axial velocity profile
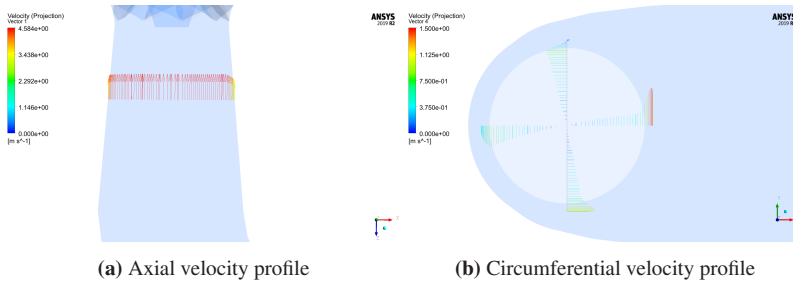

(b) Circumferential velocity profile

Figure 6.3: Velocity profiles to used to determine inlet velocity profiles for the short DT

From Figure 6.3(a), the axial velocity profile seems to be close to a uniform flow after the bend and is therefore chosen as the axial inlet velocity profile. The circumferential velocity profile looks very much like a forced vortex for $r < 0.9r_{max}$. When $0.9r_{max} < r < r_{max}$ then the circumferential velocity becomes irregular as can be seen in Figure 6.3(b). The MPM interface model which is used in the upcoming simulations, circumferential averages the velocity before the flow enters the impeller from the DT. It was therefore decided to circumferential average the values for the circumferential velocity seen in Figure 6.3(b). Based on these values, a square function from the max value at $0.9r_{max}$ to 0 for $r = r_{max}$ was chosen. The circumferential inlet velocity profile for the short DT in the following simulations can be seen in Figure 6.4. $C_{u,max}$ in Figure 6.4 was set so that the maximum circumferential velocity corresponds to the chosen angle of pre-rotation.

6.3 Sigma break curves with pre-rotation

The sigma break curve used the same definition of $\overline{\sigma}_h$ as described in section 5.1.
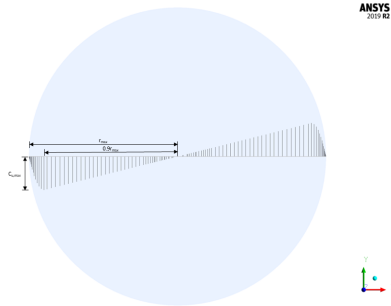
Figure 6.4: The inlet circumferential velocity on the short DT used for the simulations with pre-rotation

Low Q operating point

The simulation with $40°$ max CPR for low Q did not converge to the target residual of 10^{-6} and is therefore not taken into account in either the sigma break curve nor the pump curves in Figure 5.4 and 5.5. In Figure 6.5 it can be seen that $20°$ max CPR reduces the inception cavitation. On the contrary, counter pre-rotation increases the $\overline{\sigma}$ for both inception cavitation point in addition to the critical cavitation.
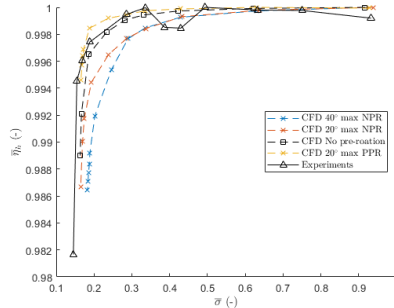
Figure 6.5: Sigma beak curve at low Q ($Q/Q_{BEP} = 0.8408$)

The required sigma value $\overline{\sigma}_R$ for this operation point is $\overline{\sigma}_R = 0.164$ without pre-rotation. $\overline{\sigma}_R = 0.170$ for $20°$ max NPR. $\overline{\sigma}_R = 0.193$ for $40°$ max NPR. $\overline{\sigma}_R = 0.151$ for the experiments. The $\overline{\sigma}_R$ for PPR is not found since the simulations did no converge when the efficiency dropped more than 1%.

BEP operating point

From the cavitation curve at BEP, Figure 6.6, it can be seen that pre-rotation has little effect on the $\overline{\sigma}_R$ for all the different pre-rotations except 40 degree positive pre-rotation which had a higher $\overline{\sigma}_R$.
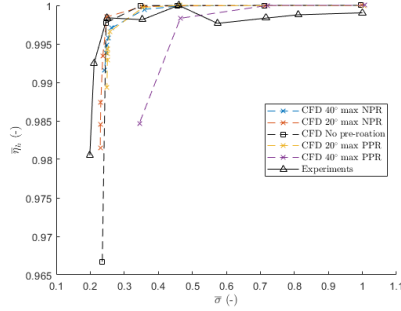

Figure 6.6: Sigma beak curve at BEP

The required sigma value $\overline{\sigma}_R$ for this operation point is $\overline{\sigma}_R \approx 0.39$ for $40°$ max PPR. $\overline{\sigma}_R = 0.250$ for $20°$ max PPR. $\overline{\sigma}_R = 0.244$ without pre-rotation. $\overline{\sigma}_R = 0.233$ for $20°$ max NPR. $\overline{\sigma}_R = 0.209$ for the experiments. The $\overline{\sigma}_R$ for $40°$ max NPR is not found due to limited simulated points around 1% drop in efficiency.

High Q operating point

The different pre-rotations had a significantly impact on the $\overline{\sigma}_R$ high Q operation point as seen in Figure 6.7. On one hand, the two cases with counter pre-rotation reduced the $\overline{\sigma}_R$ significantly. On the other hand, the two cases with positive pre-rotation had a significant increase in $\overline{\sigma}_R$. For these two it seems like higher positive pre-rotation results in higher $\overline{\sigma}_R$.

The required sigma value $\overline{\sigma}_R$ for this operation point is $\overline{\sigma}_R \approx 0.85$ for $40°$ max PPR. $\overline{\sigma}_R = 0.605$ for $20°$ max PPR. $\overline{\sigma}_R = 0.441$ without pre-rotation. $\overline{\sigma}_R = 0.331$ for $20°$ max NPR. $\overline{\sigma}_R = 0.330$ for $40°$ max NPR. $\overline{\sigma}_R = 0.412$ for the experiments.

6.4 Pump performance curves with pre-rotation

In Figure 6.8 it can be seen that the simulated operating points with both PPR and NPR results in a reduction in efficiency compared to no pre-rotation for all the simulated operating points. Of the cases with pre-rotation, $20°$ max PPR has the best efficiency for all the operating points. $20°$ max NPR is increasing in efficiency
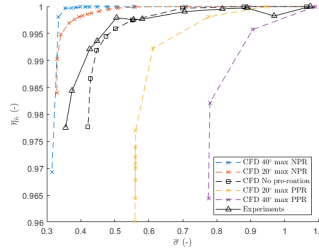
Figure 6.7: Sigma beak curve at high Q ($Q/Q_{BEP} = 1.1293$)

with increasing volumetric discharge.
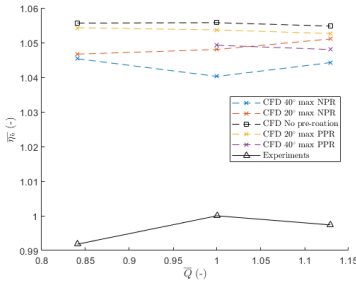
Figure 6.8: $\overline{Q} - \overline{\eta_h}$ curves with pre-rotation
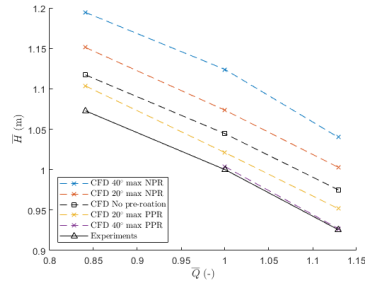
Figure 6.9: $\overline{Q} - \overline{H}$ curves with pre-rotation

As seen in Figure 6.9, the head increases with decreasing positive pre-rotation. This is as expected from the theory where Equation 2.1.

6.5   Discussion of CFD simulations with pre-rotation

In section 6.2, it is shown that secondary flows are present near the inlet of the RPT. These flows is not captured during the CFD simulations because only a single impeller and GV passage was simulated using the MPM interface model which circumferential averages the fluxes.

Although the inlet pre-rotation is an approximation of the velocity profile from a real booster pump as discussed in section 2.4, it is believed that the results presented in this chapter describes real trends associated with the effects of pre-rotation from an axial booster pump on the RPT in pump mode.

The CFD simulation at low Q operating point did not converge to the required RMS value for $40°$ max PPR. This pre-rotation and operating point is therefore not plotted in the figures. The reason for the bad convergence under these conditions was not investigated in detail, but it should be noted that a finer mesh was chosen for this operating point than the two others due to higher discretisation errors as discussed in section 4.4.

As mentioned in section 2.3, a lower σ_R does not require as high static inlet pressure as higher σ_R does. In other words, lower σ_R is desirable as the booster pump does not need to create as high pressure at the inlet in order to avoid cavitation compared to higher σ_R.

The sigma break curves showed a slight improved cavitation characteristics with positive pre rotation for low Q operating point and significant improvement with negative pre-rotation for the high Q operating point. If these pre-rotations are used, the low Q will experience a reduction in H while the high Q will experience increased H as seen in Figure 6.9. On the other side, Figure 6.8, showed that these pre-rotations reduced the efficiency of the RPT slightly for both operating conditions.

The most important simulated operating point was the high Q operating point. This was because it had the highest $\sigma_R = 0.441$ of the simulated operation points without pre-rotation. As seen in Figure 6.7, different pre-rotations changed the sigma break curve for this operating point significantly. The σ_R was reduced with 25.2% for $40°$ max NPR compared to no pre-rotation. Positive pre-rotation had the opposite effect of negative pre rotation. The σ_R increased with 93% for $40°$ max NPR compared to no pre-rotation.

The pressure coefficient is:

$$C_p = \frac{p - p_2}{\rho g H} \tag{6.1}$$

Figure 6.10 shows C_p contour and velocity vector near the LE of the impeller, high Q operating point at span 0.5. Without pre-rotation, the zone of highest pressure is leaning towards the suction side (SS) of the impeller. This is as expected for operation points above BEP as the fluid approaches the LE with a higher β than the impeller is designed for as seen in Figure 6.10. With 40 degrees max NPR, the the stagnation pressure is more in line with the LE. This results in a higher $C_{p,min}$ which explains the lower σ_R compared to no pre-rotation at this operating point as seen in Figure 6.7.
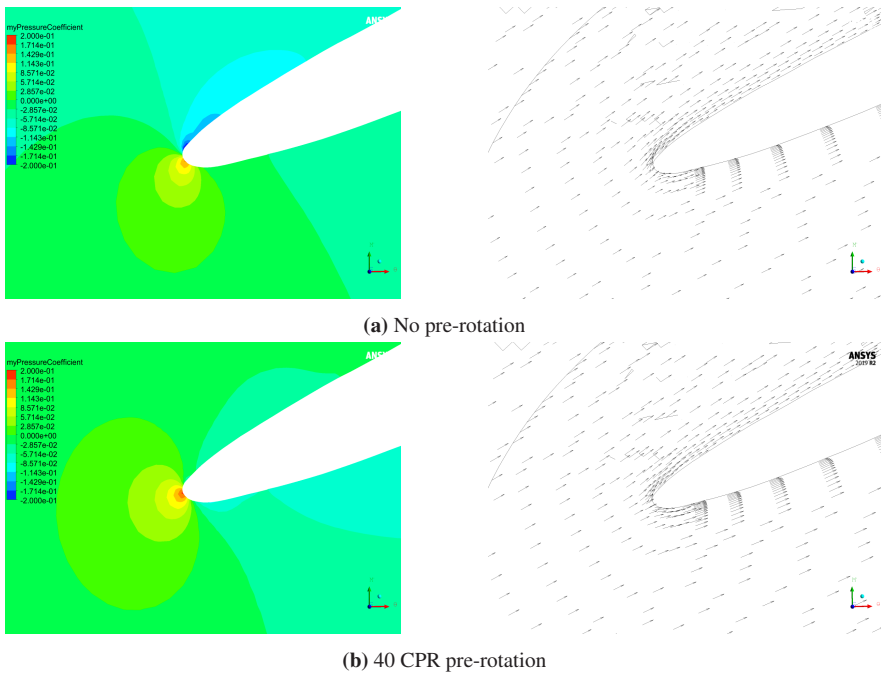
(a) No pre-rotation

(b) 40 CPR pre-rotation

Figure 6.10: Pressure coefficient and velocity vectors near LE for span 0.5 for high Q $(Q/Q_{BEP} = 1.1293)$

———————Chapter VII———————

Conclusions

Multiphase CFD simulations was successfully performed at three different operating points of the RPT. For each operating point, the pressure at the outlet was gradually reduced in order to get the sigma beak curve with the break in efficiency when cavitation is occurring. The CFD simulations had consistently a slightly higher σ_R but the trends correlated well with the experimental data. The CFD setup was therefore deemed adequate to run simulations with pre-rotation.

Pre-rotation was added by changing the inlet velocity profile to match the velocity profile of a simplified axial booster pump. For the low Q operation point, it was found that the sigma break curve had a slightly lower σ_i with 20° max PPR. For the BEP operating point, both PPR and NPR matched the results without pre-rotation closely. The exception was 40° max PPR which increased the σ_R significantly.

The high Q is the most important simulated operating point due to its high σ_R compared to the others without pre-rotaiton. Different pre-rotations significantly changes in the sigma break curve at this operating point. The simulated pre-rotations showed that the σ_R could be reduced with 25.2% with NPR and σ_R could be increased with up to 93% with PPR. In other words: 40° max NPR has the best cavitation performance because it has the lowest σ_R for this operating point. For the RPT in this thesis, NPR has a positive effect on the cavitation performance at the high Q operating point.

From the simulations with pre-rotation it was found that the efficiency was reduced for all the simulated pre-rotations, but least with the lowest angles of PPR and NPR. In addition is was found that head was increased with NPR and reduced with PPR. This correlates well with already confirmed theory regarding the analysis of pre-rotation in pumps like Liu et al. [16], Ahmed et al.[17] and Larsen [18].

If one were to induce pre-rotation from a booster pump to a RPT in pump mode

of operation, it is important to keep in mind the change in head and efficiency that follows the pre-rotation. Care should be taken when applying the findings pre-rotation has on this RPT with other RPTs because pre-rotation has different effects on machines with differing specific speeds.

—————————————— **Chapter VIII**——————————————

Further work

Simulations of a booster pump specifically designed for the RPT in this thesis should be simulated. This would provide a more realistic insight to cavitation on a RPT with an installed booster pump. The beneficial results with NPR at the operating point above BEP with respect to the sigma break curve should be kept in mind when designing the booster pump as it may be beneficial for the overall cavitation performance of the system.

Further work could include CFD simulations at operating points further away from BEP with pre-rotation. It would be interesting to see if $20°$ max CPR efficiency is continuing to increase with higher volume flows. This might require a change in the mesh and numerical setup in order to run stable simulations with high precision.

CFD simulations using the full geometry can be performed in order to get the pump performance curves to correlate better with experimental data. In addition, this might change the sigma break curves slightly compared to the simulations in this thesis due to the difference in head.

References

[1] IPCC, 2018, "Global Warming of 1.5 degreesC. An IPCC Special Report on the impacts of global warming of 1.5 degrees C above pre-industrial levels and related global greenhouse gas emission pathways, in the context of strengthening the global response to the threat of climate change, sustainable development, and efforts to eradicate poverty," In Press.

[2] Komusanac, I., Brindley, G., and Fraile, D., 2020, "Wind energy in Europe in 2019: Trends and statistics," Tech. rep., Wind EUROPE.

[3] REN21, 2019, "Renewables 2019: Global status report," REN21 Secretariat.

[4] Rogner, M. and Troja, N., 2018, "The world's water battery: Pumped hydropower storage and the clean energy transition," IHA working paper, International Hydropower Association.

[5] IRENA, 2017, "Electricity storage and renewables: Costs and markets to 2030," International Renewable Energy Agency, Abu Dhabi, p. 4.

[6] Adams, K., Taylor, R., Badinier, A., and Chuxue, L., 2019, "Hydropower status report," Tech. rep., International Hydropower Association.

[7] Rehman, S., Al-Hadhrami, L. M., and Alam, M. M., 2015, "Pumped hydro energy storage system: A technological review," Renewable and Sustainable Energy Reviews, **44**, pp. 586–598.

[8] Harby, A., Sauterleute, J., Killingtveit, A., and Solvang, E., 2015, "HYDROPOWER FOR ENERGY STORAGE AND BALANCING RENEWABLES," .

[9] HydroCen and NTNU, 2020, "Pump turbines in existing power plants," accessed 2020-06-29, `https://www.ntnu.edu/hydrocen/2.3-pump-turbines-in-existing-power-plants`

[10] Tao, R., Xiao, R., Wang, F., and Liu, W., 2018, "Cavitation behavior study in the pump mode of a reversible pump-turbine," Renewable Energy, **125**, pp. 655–667.

[11] Zhang, Y., Zhang, Y., and Wu, Y., 2017, "A review of rotating stall in reversible pump turbine," Proceedings of the Institution of Mechanical Engineers, Part C: Journal of Mechanical Engineering Science, **231**(7), pp. 1181–1204, Publisher: SAGE Publications Sage UK: London, England.

[12] Brekke, H., 2003, , Vannkraftlaboratoriet NTNU.

[13] IEC, 1999, "Hydraulic Turbines, Storage Pumps and Pump-Turbines—Model Acceptance Tests," International Electrotechnical Commission, Geneva, Switzerland, Standard No. IEC, **60193**.

[14] Gülich, J. F., 2008, *Centrifugal pumps*, 3rd ed., Springer, Berlin.

[15] Çengel, Y. A. and Cimbala, J. M., 2014, *Fluid Mechanics: Fundamentals and Applications*, 3rd ed., McGraw-HillHigher Education, Google-Books-ID: 4RVEAQAAIAAJ.

[16] Liu, Y., Tan, L., Liu, M., Hao, Y., and Xu, Y., 2017, "Influence of Prewhirl Angle and Axial Distance on Energy Performance and Pressure Fluctuation for a Centrifugal Pump with Inlet Guide Vanes," Energies, **10**(5), p. 695, Number: 5 Publisher: Multidisciplinary Digital Publishing Institute.

[17] Ahmed, S., Muiz, A., Mubashir, A., and Ahmed, W., 2016, "Efficiency enhancement of centrifugal water pump by using inlet guided vanes," European Journal of Advances in Engineering and Technology, **3**(10), pp. 1–4.

[18] Larsen, R. H., 2019, "Pre-rotation of inlet flow for a reversible pump turbine in pump mode," Accepted: 2019-10-18T14:01:13Z Publisher: NTNU.

[19] Stepanoff, A. J., 1957, *Centrifugal and axial flow pumps. Theory, Design and Application*, 2nd ed., Wiley.

[20] White, F. M., 1991, *Viscous fluid flow*, second edition ed., McGraw-Hill New York.

[21] Ytrehus, T., 2012, "The governing conservation equations in fluid mechanics," , pp. 2–16.

[22] Versteeg, H. K. and Malalasekera, W., 2007, *An Introduction to Computational Fluid Dynamics: The Finite Volume Method*, 2nd ed., Pearson Education.

[23] ANSYS CFX 2019 R2, 2019, "CFX-Solver Modeling Guide,"
`https://ansyshelp.ansys.com/account/secured?returnurl=`
`/Views/Secured/corp/v194/cfx_mod/cfx_mod.html`

[24] Plesset, M. S., 1949, "The Dynamics of Cavitation Bubbles," Journal of Applied Mechanics, **16**, pp. 277–282, Publisher: American Society of Mechanical Engineers.

[25] Fuster, D., 2019, "A Review of Models for Bubble Clusters in Cavitating Flows," Flow, Turbulence and Combustion, **102**(3), pp. 497–536.

[26] ANSYS CFX 2019 R2, 2019, "CFX Reference Guide," `https:`
`//ansyshelp.ansys.com/account/secured?returnurl=/Views/`
`Secured/corp/v194/cfx_ref/cfx_ref.html`

[27] Braun, O., 2009, "Part load flow in radial centrifugal pumps," Tech. rep., Epfl.

[28] Celik, I. B., Ghia, U., Roache, P. J., and Freitas, C. J., 2008, "Procedure for estimation and reporting of uncertainty due to discretization in CFD applications," Journal of fluids Engineering-Transactions of the ASME, **130**(7), Publisher: ASME-AMER SOC MECHANICAL ENG THREE PARK AVE, NEW YORK, NY 10016-5990 USA.

——————— **Appendix - A**———————

Nepal conference paper

Numerical simulation of cavitation on a Reversible Pump Turbine

Johan C Jenssen

Waterpower laboratory, Department of Energy and Process Engineering, NTNU, Trondheim, Norway

E-mail: `johancj@stud.ntnu.no`

Abstract. The modern power grid instabilities are increasing, arising from renewable power sources. There are a lot of different ways of stabilising the power grid, but pumped storage hydropower plants are considered to be one of the best ways of storing energy in a large scale. In these plants, it is common to have one turbine in addition to a pump. This requires two different waterways in addition to a turbine and a pump which is expensive to build. An alternative is to use a single reversible pump turbine (RPT) that can act as both a turbine and a pump.

In this paper, steady state simulation of cavitation a reversible pump turbines impeller has been successfully performed and validated using experimental data. The break in efficiency was found to happen at about the same cavitation number for both the simulations and experiments. However, the efficiency in the simulations is higher than the experimental data. This was as expected due to simplifications in the geometry in comparison with the full geometry. Further work needs to be done in order to check if the efficiency will correlate better if the full geometry including guide vanes, stay vanes, spiral casing and draft tube. Additional operating points should also be simulated in the future.

Keywords— Reversible pump turbine, cavitation, pump mode, CFD, hydropower

1. Introduction

The demand and supply in electricity does not always correlate. This is especially true for the modern grid requirements arising from renewable power sources, for example wind and solar power [4]. As a result, the modern power grid is becoming more unstable. Pumped storage hydropower plants are tested in large scales and found to be an efficient way of storing energy.

A Reversible Pump Turbine (RPT) can act as both a turbine where the hydro machinery extracts energy from the fluid and a pump where the hydro machinery adds energy to the fluid [7]. In order to contribute to make the power grid more stable, the RPT can pump water into the upper reservoirs when the demand is low and act as a turbine in order to generate power when the demand is high. RPTs are highly adaptable and can respond fast to changes in the power grid [4].

RTPs can be may be run outside its best efficiency point (BEP) which may induce unwanted cavitation. Cavitation can both reduce the RPTs efficiency in addition to increase the deterioration of the impeller thus creation a mechanical failure. Due to the consequences of cavitation, it is of great importance to be able to predict the cavitation behavior of a given RPT during the design process of RPTs. A cost-efficient way to design a pump turbine is to design it by making a 3-dimensional model of it and using numerical simulation in order to test the pump turbine numerically. The alternative it to design a pump

turbine, making a physical model and testing it in small scale. Computational fluid dynamics (CFD) reduces the need to make many physical pump turbines, thus reducing the cost of designing a pump turbine.

Cavitation is a phase shifting process which makes the CFD simulation a multiphase problem. This is computational heavy in comparison with single phase simulations due to an extra set of equations which needs to be solved every iteration.

1.1. Objectives and limitations
The objective of the work presented in this paper is to set up and test numerical simulation of cavitation on a Reversible Pump Turbines impeller in pump mode. This simulation is done at close to the RPTs BEP and compared with experimental data provided by Rainpower AS in order to validate the simulation. Limitations of this paper is mainly due to time and computer power restrictions. Consequently, the steady state CFD simulation on the impeller at a rotating frame of reference was chosen.

2. RPT characteristics
RPTs can be run both as a turbine and as a pump. The only difference between RPT in pump mode and turbine mode is the direction at which the impeller is spinning. When designing a RPT, the dimensions needs to be designed for pump mode because the head in pump mode, H_p, is larger than the head in turbine mode, H_t [2]. This is illustrated in Figure 2 and is the main reason this paper covers cavitation on a RPT in pump mode.

Euler's turbo machinery equation for RPTs in turbine mode is:

$$gH_t\eta_{ht} = (u_1c_{u1t} - u_2c_{u2t}) = E_t\eta_{ht} \tag{1}$$

where η_{ht} and H_t is the hydraulic efficiency and head in turbine mode and all the velocities is as in Figure 1. Euler's turbo machinery equation for RPTs in pump mode is given by Equation 2

$$gH_p = \eta_{hp}(u_1c_{u1p} - u_2c_{u2p}) = E_p \tag{2}$$

where η_{hp} and H_p is the hydraulic efficiency and head in pump mode and the velocities are described in Figure 1. This paper only considers an RPT in pump mode and therefore, the hydraulic efficiency in pump mode will be defined as η_h form here on out.

3. Cavitation
Cavitation is a phenomena where parts of the liquids static pressure p falls below its vapor pressure p_{va}. When cavitation is present in a domain there is two phases flow present in the domain: both liquid and vapor. If the cavitating zone is large, then the head and efficiency of the RPT may be severely compromised [3].

In pump mode, cavitation bubbles are most commonly formed at the inlet of an impeller blade, where the static pressure usually is the lowest. The bubbles are then transported through the RPT to regions where the static pressure is higher and the cavitation bobbles collapse. The collapse of the cavitation bobbles close to the physical surface of the impeller can causes a large local pressure on the surface. This effect can lead to pitting erosion on the impeller, and eventually catastrophic failure of the RPT [7, 2].

The net positive suction head ($NPSH$) is a commonly used way to assess if a hydro machinery is in risk of cavitation or not. $NPSH_A$ is the available NPSH and it is defined in Equation 3 [5].

$$NPSH_A = \frac{p_{\text{abs,in}} - p_{va}}{\rho g} \tag{3}$$

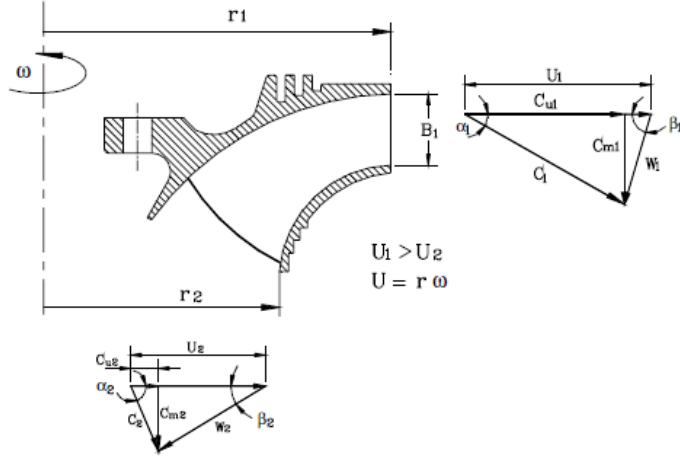where $p_{\text{abs,in}}$ is the absolute pressure at the inlet.

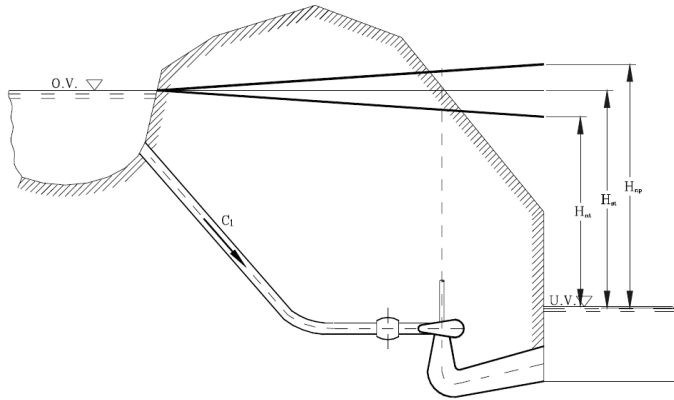**Figure 1.** Velocity triangles for RPTs. Collected from [2].

Figure 2. Difference between head in turbine and pump mode. Collected from [2].

In order to avoid cavitation, the following requirement needs to be met:

$$NPSH_A > NPSH_R \tag{4}$$

where $NPSH_R$ is the required $NPSH$ in order to avoid cavitation. There are several ways to define $NPSH_R$, but a common way is to define it at when the efficiency has dropped 1% due to cavitation, $NPSH_1$.

3.1. Sigma break curves

The Thoma cavitation number, σ, is a dimensionless term indicating the conditions of cavitation under which the machine operates [5] and is defined in Equation 5.

$$\sigma = \frac{NPSH_A}{H} \tag{5}$$

where H is the head. Similarly to the $NPSH_R$ can be set to be $NPSH_1$, the cavitation number σ_1 can be defied based on the $NPSH_1$.

The sigma break curve is a chart where usually either the cavitation number, σ, or the $NPSH_A$ is plotted along the x-axis and efficiency is plotted along the y-axis. From this chart it is possible to judge at under which conditions cavitation will appear for a RPT. The sigma break curve will therefore be used in order to validate the CFD results to the experimental data.

4. CFD setup
It was decided to use the CFD software Ansys Turbogrid for the meshing of the impeller and Ansys CFX for the simulations.

4.1. Geometry
The Geometry is kindly provided by Rainpower AS. They have also provided the author with their experimental data for this geometry under different operating conditions for cavitation. This geometry is confidential and all parameters will therefore be relative. The only part of the geometry used in this paper is the impeller. It was decided to only use this part of the geometry in order to reduce computational time and to verify the numerical setup early.

4.2. Mesh
The mesh of the impeller was created using Ansys Turbogrid. The mesh was designed for a $k-\epsilon$ turbulence model with a wall y+ value of 30 and a maximum expansion rate of 1.2. Structured hexahedral mesh was generated and it had $\sim$ 1.1 million cells for a single passage. The mesh statistics can be found in Table 1.

Table 1. Mesh statistics

Mesh attribute	Value
Minimum face angle	28.79 $[degree]$
Maximum face angle	151.24 $[degree]$
Maximum element volume ratio	3.22
Maximum aspect ratio	91.68

The mesh statistics in Table 1 is well within the general advise from Ansys [1] and the mesh is therefor considered to be a good mesh. The general advise from Ansys CFX is:

- 10 [degree] < Face angle < 170 $[degree]$

- Element volume factor < 20

- Aspect ratio < 100

4.3. Numerical setup
It was decided to use a robust and computational cheap numerical setup in order to get to some results fast. The following setup was chosen:

- The standard $k-\epsilon$ turbulence model was chosen because of its good reputation from the industry for being a stable turbulence model. This turbulence model was found to be a good compromise between speed and accuracy. The $k-\epsilon$ model uses wall functions thus it requires a less fine mesh than turbulence models like the SST model, that do not use wall functions [6, 3].

- "High Resolution" advection scheme for both continuity and momentum equations. This scheme was chosen because of the precision and stability of this scheme.

- "Upwind" advection scheme for turbulence eddy dissipation and turbulence kinetic energy equations as suggested by Ansys [1].

- Steady-state was chosen in order to simplify the problem and thus making it less computational heavy.

- Single, rotating frame of reference on the impeller. No rotor-stator interactions.

- Single phase initialisation, then multiphase simulations for different cavitation numbers according to the experimental data. p_{va} was computed by linear interpolation for the exact temperature from the experimental data.

- Rotational periodicity interface on a single passage of impeller. This reduces the computational time a lot by simulating only a single passage.

- Physical timescale according to 1 degree of rotation per timescale.

- Boundary conditions:
    - Inlet: constant total pressure in stationary frame of reference, corresponding to the desired cavitation number, 5% turbulence intensity at the inlet.
    - Outlet: constant mass flow based on the averaged mass flow from the experimental data.
    - Walls: No slip, smooth wall.

The numerical simulation was considered to be converged when the root mean square residuals (RMS) was below 10^{-6}.

5. Results

The CFDs hydraulic efficiency, $\overline{\eta}_{h,\text{CFD}}$, will be normalised based on the best efficiency for the current CFD run. Likewise, the experimental hydraulic efficiency, $\overline{\eta}_{h,\text{exp}}$, will be normalised based on the best efficiency for the current experimental data set. The normalised efficiency is defined in Equation 6.

$$\overline{\eta}_h = \frac{\eta_h}{\eta_{h,\text{best efficiency}}} \tag{6}$$

Similarly to the normalised efficiency, a normalised cavitation number, $\overline{\sigma}$, is defined in Equation 7 for both CFD and the experimental data based on the highest σ value of the experiments data set.

$$\overline{\sigma} = \frac{\sigma}{\sigma_{\text{a defined value}}} \tag{7}$$

After running the simulation, it is found that $\frac{\eta_{h,\text{CFD}}}{\eta_{h,\text{exp}}} = 1.0701 \approx 7\%$. It is expected that the CFD simulation was going to have a higher efficiency than the experimental data due to the lack of losses in the draft tube, guide vanes, stay vanes and spiral casing.

Figure 3 shows the preliminary results with the mesh and the numerical setup described in section 4. The break in efficiency happens at about $\overline{\sigma}_{\text{CFD}} \approx 0.251$ for the CFD results and $\overline{\sigma}_{\text{exp}} \approx 0.249$ for the experiments. This is very close to each other and is considered to be the same due to the lack of data points close to this position. A commonly used definition of critical cavitation point of 1% loss in efficiency and described as σ_1. In this case, we get the following approximate results: $\overline{\sigma}_{1,\text{CFD}} \approx 0.23$ and $\overline{\sigma}_{1,\text{exp}} \approx 0.21$.

Figure 4 and Figure 5 illustrates the location at which cavitation is occurring on the impeller. It can be observed that cavitation happens on both sides of the impeller which indicates that the RPT is close to its best efficiency point.
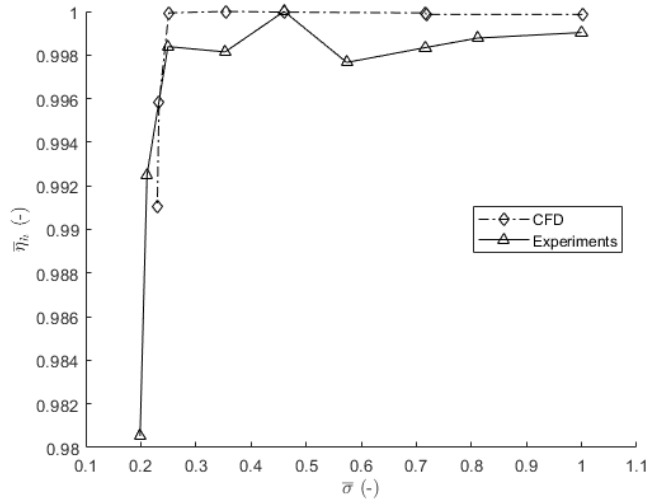
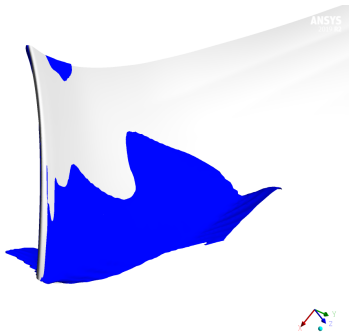**Figure 3.** Sigma break curve for CFD and experimental data.

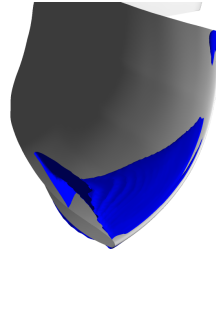**Figure 4.** Cavitation on the impeller at the suction side.

Figure 5. Cavitation on the impeller at the pressure side.

6. Conclusion

The mesh parameters is good according to the general advise from Ansys [1]. Despite of this, a mesh independence study should be performed in order to validate the performance of the mesh. However, because the break point of the sigma break curve in Figure 3 it is shown that the CFD results correlates well compared to the experimental data. Therefore, the mesh is considered to have a sufficiently good quality despite the lack of mesh impedance studies.

The overall results is promising despite the $\sim 7\%$ higher efficiency in the simulations compared to the experiments. The simplified CFD geometry does not take losses between the inlet of the draft tube and the outlet of the spiral casing and setup into account. The increased efficiency in the simulation is as expected due to the reduced losses due to the simplified geometry.

The break in efficiency in Figure 3, happens for about the same $\overline{\sigma}$ values for both the CFD simulations

and the experimental data. This means that the CFD simulation is validated, thus the numerical setup is therefore considered to be good for this operation point. Due to the good result, the numerical setup will create a solid base to start increasing the complexity of the simulations in the future.

7. Further Work

A mesh impedance study should be performed in order to validate the mesh. However, this is not a requirement as long as the simulated results are validated using experimental data. More operating points should be simulated and validates. In order to achieve more accurate results at different operating points, the geometry needs to include the entire geometry including the draft tube, guide vanes, stay vanes and the spiral casing. This will probably additionally make the simulated efficiency closer to the efficiency according to the experimental data. Simulations adding pre-rotation to the inlet should also be performed in order to check if pre-rotation has a significant advantage/disadvantage on the RPT in pump mode of operation outside the normal best efficiency operation.

References

[1] ANSYS. Ansys cfx 2019 r2, cfx-solver modeling guide, 2019.
[2] H. Brekke. Pumper & turbiner. *Vannkraftlaboratoriet NTNU*, 2003.
[3] J. F. Gülich. *Centrifugal pumps*, volume 2. Springer, 2008.
[4] IHA. Hydropower status report. 2019.
[5] I. Standard et al. Hydraulic turbines, storage pumps and pump-turbines—model acceptance tests. 1999.
[6] H. K. Versteeg and W. Malalasekera. *An Introduction to Computational Fluid Dynamics*. Pearson Education Limited, 2 edition, 2007.
[7] Y. A. Çengel and J. M. Cimbala. *Fluid Mechanics: Fundamentals and Applications*. McGraw-Hill Education, 3 edition, 2014.